Journal of Materials Chemistry A

ROYAL SOCIETY OF CHEMISTRY

PAPER

View Article Online
View Journal | View Issue

Cite this: J. Mater. Chem. A, 2023, 11, 22960

Enhancement of thermoelectric properties of $CuFeS_2$ through formation of spinel-type microprecipitates†

Sahil Tippireddy, ‡[a] Feridoon Azough,[b] Animesh Bhui,[c] Iuliia Mikulska,[d] Robert Freer, [b] Kanishka Biswas, [c] Paz Vaqueiro [a] and Anthony V. Powell *[a]

$CuFeS_2$ (chalcopyrite) is a promising n-type thermoelectric candidate for low-grade waste heat recovery. In this work, chromium-containing $CuFeS_2$ materials of general formula $Cu_{1-x}Cr_xFeS_2$ ($0.0 \leq x \leq 0.1$) were prepared *via* solid-state synthesis. Efforts to substitute chromium in $CuFeS_2$ leads to the preferential formation of a composite, in which lamellar precipitates of a Cr-rich, spinel-type $[Cu,Fe,Cr]_3S_4$ phase, are embedded in the unsubstituted $CuFeS_2$ matrix. X-ray absorption near-edge spectroscopy (XANES) reveals that the electronic structure of copper, iron and sulfur in the principal $CuFeS_2$ phase remains unaltered by chromium incorporation. However, the formation of $[Cu,Fe,Cr]_3S_4$ precipitates alters the Cu : Fe ratio of the $CuFeS_2$ phase, producing a change in the net carrier concentration through reduction of a portion of Fe^{3+} ions to Fe^{2+}. The chromium content of the spinel precipitates determines the extent of the change in the Cu : Fe ratio of the main $CuFeS_2$ phase, and hence, indirectly affects the electrical properties. The micro/nanometre-sized $[Cu,Fe,Cr]_3S_4$ precipitates and nanoscale dislocations enable a broad spectrum of heat-carrying acoustic phonons to be scattered, resulting in a significantly reduced lattice thermal conductivity. Combined with an enhanced power factor, a maximum thermoelectric figure-of-merit, zT of 0.31 at 673 K is achieved for the $x = 0.08$ sample; a three-fold increase over that of the pristine phase.

Received 21st August 2023
Accepted 10th October 2023

DOI: 10.1039/d3ta05011d

rsc.li/materials-a

Introduction

Thermoelectric materials, capable of converting heat into electricity, have received widespread interest for their ability to generate useful electrical energy from otherwise waste heat in a range of applications.[1] The thermoelectric conversion efficiency depends on the figure-of-merit, defined as $zT = S^2T/\rho\kappa$; where S, ρ, κ and T represent the Seebeck coefficient, electrical resistivity, thermal conductivity and temperature, respectively. The thermal conductivity has contributions from both charge carriers (κ_e) and lattice vibrations (κ_L). For large-scale applications, it is essential to design and synthesize thermoelectric materials containing cheap, abundant and non-toxic elements. This has motivated a large body of research into binary and higher order copper-sulfides.[2–4] Whilst this has resulted in significant improvements in the thermoelectric performance of p-type sulfide materials,[5–12] that of n-type analogues remains relatively low.[13–16]

$CuFeS_2$ (chalcopyrite) is a promising n-type thermoelectric material[17] which offers a cost-effective and environmentally-friendly alternative to conventional materials such as PbTe,[18,19] Bi_2Te_3 (ref. 20 and 21) and SnSe.[22] However, the figure-of-merit of $CuFeS_2$ is relatively low, owing to its moderate power factor and high lattice thermal conductivity.[2,23–26] Previous studies have shown that substitution of Cu^+ with higher oxidation state cations is an effective means of optimizing the carrier concentration, while reducing the lattice thermal conductivity.[23,26–30] In particular, substitution with dipositive transition-metal cations leads to substantial improvements in the power factor (S^2/ρ) due to optimization of the carrier

[a]Department of Chemistry, University of Reading, Whiteknights, Reading, RG6 6DX, UK. E-mail: a.v.powell@reading.ac.uk

[b]Department of Materials, University of Manchester, Manchester, M13 9PL, UK

[c]New Chemistry Unit, Jawaharlal Nehru Centre for Advanced Scientific Research, Jakkur, Bangalore 560064, India

[d]Diamond Light Source, Harwell Science and Innovation Campus, Didcot, OX11 0DE, UK

† Electronic supplementary information (ESI) available: Lattice parameters; first derivative of the XANES absorption ($\mu(E)$) spectra of Cu, Fe, S, Cr in $Cu_{0.92}Cr_{0.08}FeS_2$ and XANES K-edges of all elements in $Cu_{1-x}Cr_xFeS_2$ ($0 \leq x \leq 0.1$) samples; sulfur absorption spectra for $Cu_{1-x}Cr_xFeS_2$ ($0 \leq x \leq 0.1$) and FeS_2; SEM images; calculation of the balanced equations and determination of the elemental content and Cu : Fe ratio in the main phase; analytically-determined composition of the main phase; dependence of Cr content and 1/Cu in the spinel secondary phase on the Cu : Fe ratio in the main phase as a function of nominal Cr concentration; room temperature Hall measurement data; calculation details to determine the Lorenz number and resulting values, mean and average sound velocity, shear and Young's moduli and Debye temperature. See DOI: https://doi.org/10.1039/d3ta05011d

‡ Present address: Diamond Light Source, Harwell Science and Innovation Campus, Fermi Ave, Didcot, OX11 0DE, United Kingdom.

concentration.[23,26,28] However, with the exception of a few studies,[31–33] there has been a general lack of progress in achieving significant reductions in the lattice thermal conductivity. More generally, Liu *et al.*[34] have suggested that glass-like thermal conductivities may be achieved in materials in which there are partially occupied crystallographic sites. A wide range of strategies to effect reductions in thermal conductivity have been reviewed by Ghosh *et al.*[35] In the case of chalcopyrite, it has been shown recently that the substitution of *p*-block elements such as germanium and indium at the cation sites, introduces a local structural distortion, resulting in enhanced point defect phonon scattering and lattice softening.[30–32] Line defects such as dislocations and twinning have also been reported to be beneficial in scattering the heat-carrying acoustic phonons.[29,30] Theoretical calculations using density functional theory (DFT) reveal that most of the heat-carrying acoustic phonons in $CuFeS_2$ have mean-free paths in the range of 50 to 500 nm.[29,36] Formation of nanocomposites targeting these length scales, therefore, offers an effective strategy for achieving low lattice thermal conductivities. This has been implemented in many materials through a variety of approaches, including spinodal decomposition,[37–39] eutectic decomposition,[40–42] nucleation and growth,[43–45] and matrix encapsulation,[46,47] leading to enhanced thermoelectric performance. However, these methods generally require careful heat treatments, rapid cooling/quenching, extensive post synthesis processing, composition tuning or a combination of two or more of these. Although there have been reports of nanostructuring *via* chemical synthesis[48–50] or mechanical alloying,[51,52] efforts to achieve multi-phase nano/micro composites in chalcopyrite are generally lacking. However, it has been reported that substitutions of Zn[23] and Pd[26] at the Cu site in $CuFeS_2$ may lead to the formation of precipitates, enabling lowering of the thermal conductivity.

In this work, we sought to substitute chromium for copper through the preparation of materials of general formula, $Cu_{1-x}Cr_xFeS_2$ ($0.0 \leq x \leq 0.1$). Chromium is an attractive choice for a substituent as it can adopt a range of oxidation states in transition-metal based sulfides, including +2 (CrS),[53] +3 (Cr_2S_3,[53] MCr_2S_4; M = Cu, Fe, Zn, Cd, Ni, V[53–57]), mixed +2/+3 (Cr_3S_4)[58] and mixed +3/+4 ($CuCr_{1-x}V_xS_2$; $x = 0$–0.4)[59] offering opportunities to effect large changes in carrier concentration. However, results from a variety of state-of-the-art characterization techniques demonstrate that the introduction of chromium preferentially leads to the formation of micro/nano-sized precipitates of a Cr-rich spinel-type phase within a matrix of unsubstituted $CuFeS_2$. The formation of this micro-composite is achieved *via* standard solid-state synthesis, without the need for any special thermal treatment. The formation of the Cr-rich spinel induces a change in the Cu : Fe ratio of the parent $CuFeS_2$ phase, altering the carrier concentration and therefore, the electrical-transport properties. In addition, the wide range of length scales of the spinel precipitates leads to enhanced scattering of heat-carrying acoustic phonons, resulting in a significant reduction of the lattice thermal conductivity. The changes to the electrical and thermal transport properties, thus, contribute to a significant increase in the figure of merit.

Experimental details

Elemental copper (Sigma-Aldrich, 99.5%), iron (Alfa Aesar, 99%+), chromium (Fisher Scientific, 99.999%) powders and sulfur flakes (Sigma-Aldrich, 99.99%) were mixed in stoichiometric amounts according to the general formula, $Cu_{1-x}Cr_xFeS_2$ ($0.0 \leq x \leq 0.1$) and sealed in evacuated ($\sim 10^{-3}$ mbar) fused silica tubes. The tubes were heated to 723 K, held at this temperature for 150 hours and then cooled at 0.4 K min^{-1} to room temperature. The products were ground to fine powders using an agate mortar and pestle and re-fired in evacuated fused silica tubes at 1173 K for 48 hours, before cooling to room temperature at 0.4 K min^{-1}. The powders were then re-ground and hot pressed at 873 K for 30 minutes under a pressure of 80 MPa to produce disc shaped pellets (diameter $\sim$ 13 mm, thickness $\sim$ 1.5–2 mm). The densities of the hot-pressed pellets determined by the Archimedes method, using an AE Adam PW 184 balance, are >98% of the crystallographic value.

Powder X-ray diffraction (PXRD) data for the hot-pressed samples were collected using a Bruker D8 Advance diffractometer (Cu $K_{\alpha 1}$: $\lambda = 1.5405$ Å). Rietveld refinement using the PXRD data was performed using Fullprof software.[60] A SIRION FEI FEG-SEM was used to perform scanning electron microscopy (SEM), and energy-dispersive X-ray spectroscopy (EDS) elemental point analysis was carried out using a TESCAN MIRA LC FEG-SEM equipped with an Oxford Instrument SDD energy dispersive detector. High-resolution transmission electron microscopy (HRTEM) and selected area electron diffraction (SAED) was carried out using a FEI Tecnai G2 FEGTEM.

X-ray absorption near edge spectroscopy (XANES) of $Cu_{1-x}Cr_xFeS_2$ ($0 \leq x \leq 0.1$) was performed on the B18 beamline[61] at the Diamond Light Source synchrotron facility, UK. Sulfur (2472 eV), chromium (5989 eV), iron (7112 eV) and copper (8979 eV) K-edge XANES measurements were performed at room temperature using Quick-EXAFS technique. A Si (111) double crystal monochromator was used to select the incident X-ray energy. Chromium, iron and copper K-edge XANES spectra were recorded using a platinum-coated collimating mirror, while for measurements of sulfur K-edge spectra, a collimating mirror with a chromium coating was used. The rejection of higher harmonics was achieved by using two dedicated platinum-coated mirrors in the case of chromium, iron and copper K-edge measurements and nickel-coated mirrors for the sulfur K-edge. Powder samples for chromium, copper and iron K-edge XANES measurements were mixed with cellulose and ground to a fine powder in a mortar and pestle. *Ca.* 100 mg of each mixture was cold pressed using a stainless-steel die and plunger to make a thin pellet of 13 mm diameter for each composition. For measurements of sulfur K-edge XANES spectra, the powder samples were spread on one side of double-sided adhesive carbon tape and the tape stuck to the aluminium sample holder using the other side of the tape. The copper and iron spectra were collected in transmission mode, whereas chromium spectra were collected in the fluorescence mode using a Canberra 36 pixel Monolithic Segmented Hyper Pure Germanium Detector (HPGe). The sulfur spectra were collected in the total electron yield mode in order to minimize the self-absorption

effect. For energy calibration, copper, iron and chromium reference foils and sulfur elemental powder were used. Since chromium is present in very low amounts, a total of 25 data collections were required to collect the chromium spectra for each chromium-containing sample, while 4–6 collections were performed to obtain the copper, iron and sulfur spectra. A set of standards consisting of copper, iron, chromium, sulfur, $NiCr_2S_4$, VCr_2S_4, Cr_3S_4, $LiFeO_2$, FeS_2, Cr_2O_3, Cu_2O and Cr_3S_4 was also measured (each 5–6 data collections) to aid assignment of oxidation states in the chromium-containing materials. The data calibration, normalization and processing, including merging the data from multiple runs, was performed using the Athena software.[62] The absorption edge energies were then extracted and compared with that for pristine $CuFeS_2$ (in which the oxidation states of the elements are well established from X-ray photoelectron spectroscopy),[23,29,63–65] and those from the standards, in order to determine the oxidation states of copper, iron, sulfur and chromium in the Cr-containing samples.

Electrical resistivity and Seebeck coefficient measurements ($323 \leq T/K \leq 723$) of hot-pressed pellets of $Cu_{1-x}Cr_xFeS_2$ were carried out using a Linseis LSR-3 system. An Ecopia HMS-3000 system was used for Hall effect measurements at room temperature. Thermal diffusivity measurements were carried out using a Netzsch LFA-447 NanoFlash ($323 \leq T/K \leq 573$) and an Anter Flashline-3000 ($573 \leq T/K \leq 673$ K). The thermal conductivity was then determined from $\kappa = \alpha C_p d$, where α denotes the thermal diffusivity, C_p (taken as the Dulong–Petit value of 0.52 J g^{-1} K^{-1}) is the specific heat capacity, and d is the sample density. The longitudinal (v_l) and transverse (v_t) sound velocities for disc-shaped hot-pressed pellets were measured using an Epoch 650 Ultrasonic Flaw Detector (Olympus) with a transducer frequency of 5 MHz.

Results and discussion

PXRD data for $Cu_{1-x}Cr_xFeS_2$ ($0 \leq x \leq 0.1$) (Fig. 1a) can be indexed on the basis of a tetragonal unit cell (space group: $I\bar{4}2d$), confirming the presence of the chalcopyrite-type phase at all compositions. A weak peak, observable as a shoulder on the main (112) peak of the chalcopyrite phase, appears to be consistent with the presence of a secondary $[Cu,Fe,Cr]_3S_4$ spinel-type phase, identified by electron microscopy (*vide infra*). Rietveld refinement (Fig. 1b) reveals that this spinel-type secondary phase is present in very low amounts (<5 vol%) with the majority of the sample consisting of the $CuFeS_2$ chalcopyrite phase. The lattice parameters (inset to Fig. 1b) are relatively invariant as a function of chromium concentration. This provides a first indication that chromium might not be substituting for copper in chalcopyrite but may be forming a secondary phase. The lattice parameter trend also suggests that unlike other transition metals,[23,26–28] the solubility limit of chromium in $CuFeS_2$ chalcopyrite is either very low (less than 2 at%) or negligible.

To investigate further the nature of chromium incorporation in materials of nominal composition $Cu_{1-x}Cr_xFeS_2$, XANES spectra were collected for each composition (Fig. 2). The absorption edge energies were extracted from the maxima in the derivative of XANES spectra (shown in Fig. S1† for $Cu_{0.92}Cr_{0.08}FeS_2$). The energies of the copper, iron and sulfur absorption edges for all the samples (Table S2†) are similar and, on the basis of comparison with pristine $CuFeS_2$, oxidation states of +1, +3 and −2 can be assigned to Cu, Fe and S, respectively. The similarity of the spectra with a negligible shift in the K-edge energies (Fig. 2) suggests that the introduction of chromium does not significantly alter the oxidation states of the elements in the main chalcopyrite phase. In addition, the similar profiles of the copper, iron and sulfur XANES spectra for all the Cr-containing materials and that of the pristine phase indicates that there is no significant change in the electronic structure or the local bonding and coordination environment in the main chalcopyrite phase on the addition of chromium. However, for the pristine sample, there are additional weak features at 2472 and 2483 eV in the sulfur spectra which can be attributed to a FeS_2 secondary phase (Fig. 2c and S2†), the

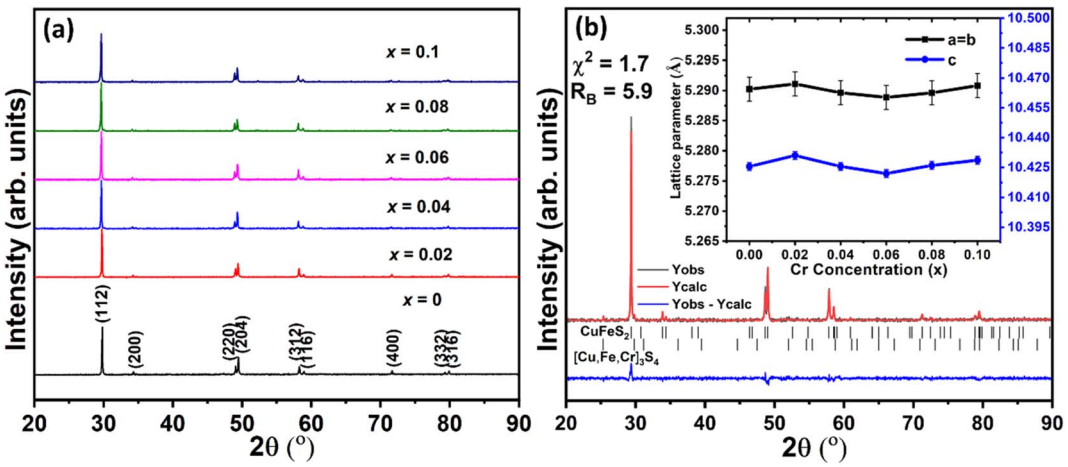

Fig. 1 (a) Powder X-ray diffraction (PXRD) data for $Cu_{1-x}Cr_xFeS_2$ ($0 \leq x \leq 0.1$). (b) Rietveld refinement using data for the $x = 0.08$ sample. Reflection positions of the main (chalcopyrite) phase and secondary spinel-type phase are marked. The inset illustrates the relative invariance of the lattice parameters of the chalcopyrite phase with chromium concentration.

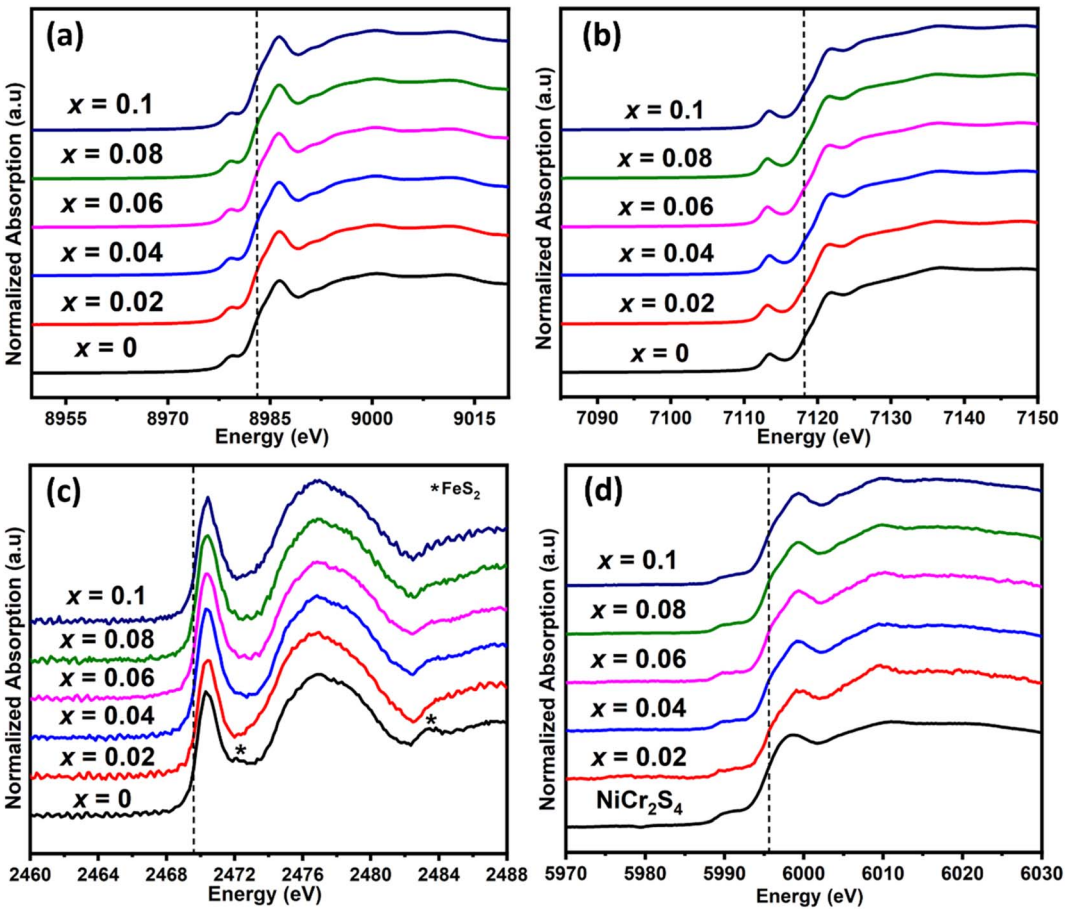

Fig. 2 K-edge XANES spectra for (a) copper (b) iron (c) sulfur and (d) chromium in $Cu_{1-x}Cr_xFeS_2$ ($0 \leq x \leq 0.1$) samples. Spectra are shifted vertically for clarity.

presence of which in the pristine phase has been previously established.[29,30] The energy of the absorption edge and the profile of the chromium spectra in the Cr-containing samples (Fig. 1d) is similar to that in the chromium spectrum of the $NiCr_2S_4$ standard, suggesting that chromium is present in the +3 oxidation state, in an octahedral coordination with sulfur atoms.[57] Together with the identification of a cubic phase by powder X-ray diffraction and TEM (*vide infra*), this provides strong evidence that the introduction of chromium leads to the formation of a $[Cu,Fe,Cr]_3S_4$ spinel-type phase, in preference to a chromium-substituted chalcopyrite phase.

Scanning electron microscopy (SEM) images of all Cr-containing materials, provided in Fig. S3† (the microstructural characterization for $x = 0$ sample is available in Tippireddy *et al.*[30]), show micro-sized precipitates of a secondary phase within the chalcopyrite matrix. These precipitates possess lamellar-like features similar to PbTe-based composites[66,67] and have not been observed in other substituted $CuFeS_2$ compounds. Fig. 3 shows the EDS maps for $x = 0.04$ and 0.08 samples which reveal that these precipitates are composed of a Cr–S rich phase. The EDS maps also reveal that there is negligible chromium present in the main $CuFeS_2$ chalcopyrite phase, confirming that chromium is incorporated into a secondary phase and not as a substituent in the chalcopyrite phase, in agreement with the results of PXRD and XANES. The composition of the secondary phases determined by EDS (Table S3†), reveals an off-stoichiometric Cr-rich M_3S_4 (M = Cu, Fe, Cr) compound with a varying degree of chromium content. Zub *et al.*[54,55] reported that $Cu_mFe_{1-m}Cr_2S_4$ ($0 \leq m \leq 0.1$) spinels can retain their structure over a wide range of stoichiometries. The stoichiometry of thiospinels of this type has been shown to be sensitive to cationic substitutions and synthesis conditions, forming off-stoichiometric $Cu_mFe_nCr_{2-l}S_4$ type compositions (with m, n and l deviating from nominal values),[54] similar to the spinel secondary phases in the present work. The HRTEM images of the $x = 0.08$ compositions (Fig. 4) clearly show the presence of Cr-rich grains within the chalcopyrite matrix. Moreover, the SAED patterns of these Cr-rich grains correspond to the $Fd\bar{3}m$ cubic structure, again consistent with the formation of a spinel-type phase indicated by PXRD and XANES. Hence, based on the PXRD, SEM, HRTEM, SAED and EDS results, the secondary lamellar-like phase is identified as a Cr-rich $[Cu,Fe,Cr]_3S_4$ spinel-type phase, whereas the main phase is unsubstituted $CuFeS_2$. Efforts to substitute chromium for copper in chalcopyrite therefore, result in an unusual phase segregation and formation of a composite containing micro

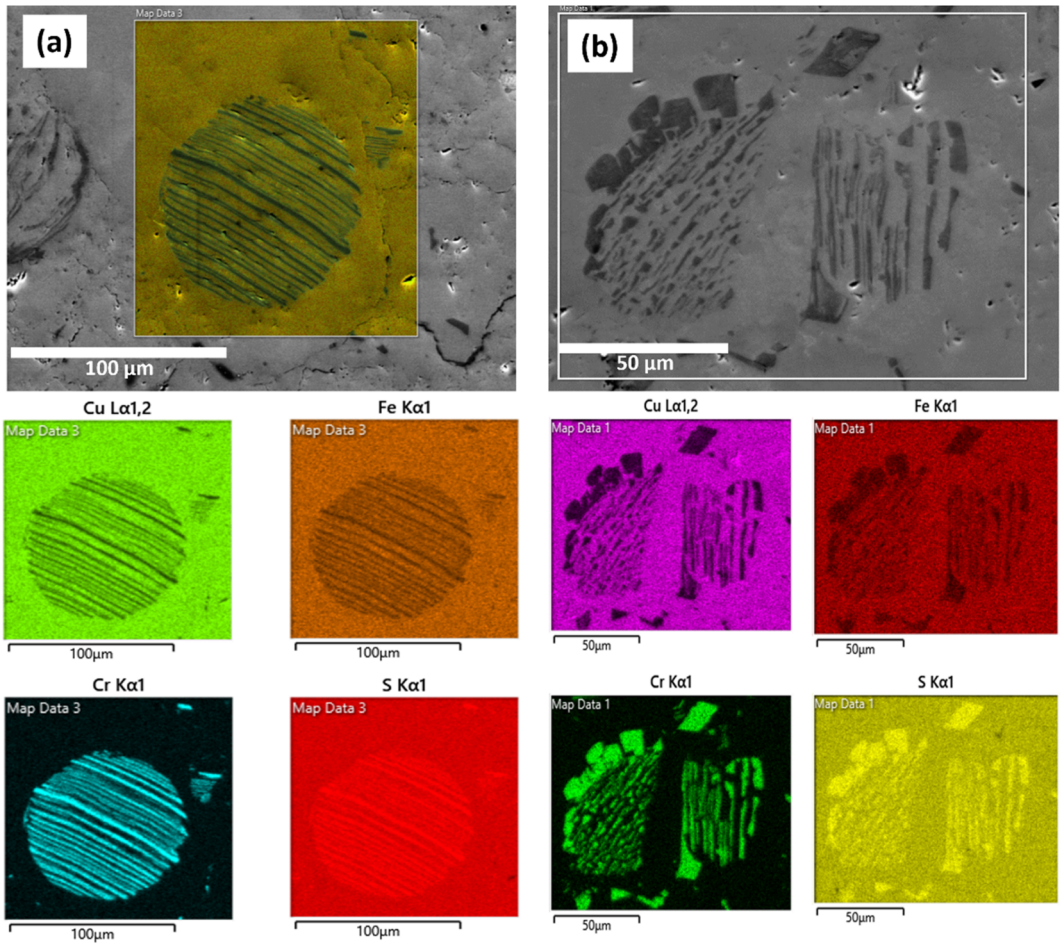

Fig. 3 Scanning electron microscopy (SEM) images with corresponding EDS area mapping of (a) $x = 0.04$ and (b) $x = 0.08$ compositions.

precipitates possessing a different structure to that of the majority-phase matrix. Moreover, this composite formation is induced even at very low levels of chromium substitution (2 at%). Understanding the origin of the tendency for chromium to form microprecipitates in preference to substitution into the chalcopyrite matrix, would require a detailed investigation of the kinetics and thermodynamics of the processes involved, including a comprehensive survey of the quaternary phase diagram. However, it is possible that the presence of chromium in the +3 oxidation state plays a role, as Cr^{3+} generally occurs in an octahedral geometry, as in the thiospinel microprecipitates, and does not favour the tetrahedral coordination adopted by the cations in chalcopyrite.

Since the nominal composition of the Cr-containing samples is $Cu_{1-x}Cr_xFeS_2$ ($0 \leq x \leq 0.1$), the formation of the microprecipitates requires a slight change in the Cu : Fe ratio of the main $CuFeS_2$ chalcopyrite phase to maintain elemental balance. Based on the characterization results discussed above, a qualitative analysis is performed to understand the change in the Cu : Fe ratio in the main chalcopyrite phase and how it may affect the carrier concentration and transport properties. For example, in the case of the nominal composition of $Cu_{0.98}Cr_{0.02}FeS_2$, which produces a chalcopyrite-type and a spinel-type phase, a balanced equation (assuming stoichiometric sulfur) can be expressed as:

$$Cu_{0.98}Cr_{0.02}FeS_2 = bCu_xFe_yS_2 + cCu_uFe_vCr_wS_4 \quad (1)$$

The calculated balanced equations for all Cr-containing $Cu_{1-x}Cr_xFeS_2$ ($0 \leq x \leq 0.1$) phases are presented in the ESI (Table S3).† Of particular note is that the Cu : Fe ratio in the majority chalcopyrite phase is reduced by between 1 and 9% from the ideal ratio of 1.0, primarily due to a decrease in the copper content. The Cu : Fe ratio initially decreases in the compositional range $0.02 \leq x \leq 0.06$, increases at $x = 0.08$, before again decreasing with further addition of Cr ($x = 0.1$). While such small changes of <9% in the Cu : Fe ratio are not discernible in the experimental EDS data, they are likely to have significant implications for the transport properties, as has been observed previously.[48,68] Since the formal oxidation states of copper, iron and sulfur in $CuFeS_2$ are +1, +3 and −2 respectively,[23,29,63–65] the partial replacement of copper by iron drives the Cu : Fe ratio below 1.0. This therefore requires reduction of a fraction of the Fe^{3+} cations to Fe^{2+} in order to maintain the charge neutrality, similar to what has been observed in $Cu_mFe_{1-m}Cr_2S_4$ spinels.[54,55] This introduces holes,

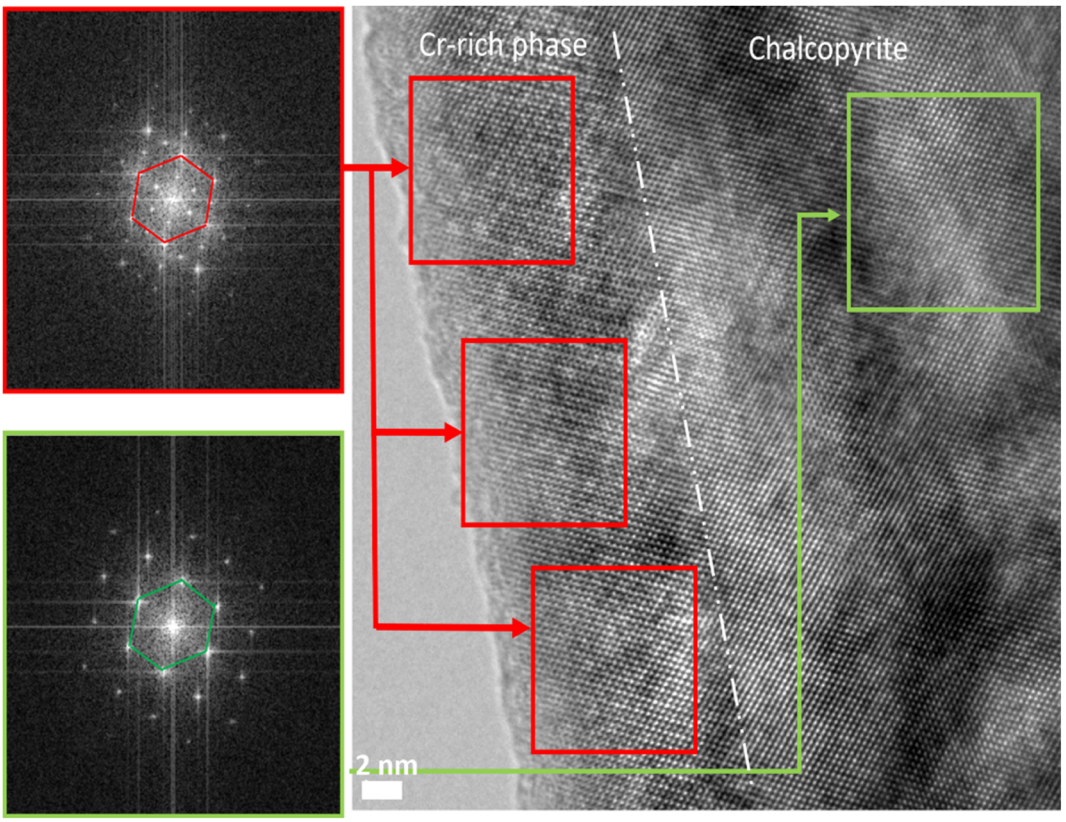

Fig. 4 HRTEM image and SAED patterns along the [110] zone axis showing the presence of spinel grains within the chalcopyrite matrix in the sample with $x = 0.08$. The white dashed line represents the interface between the two phases.

thereby reducing the net charge carrier concentration and affecting the transport properties accordingly. Since only a small fraction of Fe^{3+} ions are converted to Fe^{2+}, the change in overall oxidation state is below the limit of detection by XANES, although it is sufficient to modify the charge carrier concentration and hence the transport properties.

Hall-effect measurements (Fig. 5) for $Cu_{1-x}Cr_xFeS_2$ ($0 \leq x \leq 0.1$) reveal that the charge-carrier concentration (n) for the composition with $x = 0.02$ is increased relative to $CuFeS_2$.

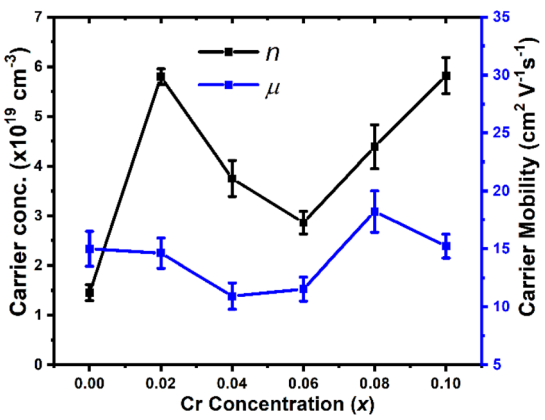

Fig. 5 Carrier concentration and mobility as a function of chromium concentration in $Cu_{1-x}Cr_xFeS_2$ ($0 \leq x \leq 0.1$).

However, n decreases in the compositional range $0.02 < x \leq 0.06$, before increasing again for compositions in the range $0.06 < x \leq 0.1$. This apparent non-systematic dependence of carrier concentration on the chromium content can be rationalised in terms of the change in Cu : Fe ratio of the chalcopyrite phase, induced by the precipitation of chromium-rich spinels. A lower Cu : Fe ratio leads to more Fe^{2+} ions and a larger concentration of holes. This results in a lower net carrier concentration as shown in Fig. 6, where the variation of the Cu : Fe ratio shows a strong correlation with the carrier concentration determined from Hall effect measurements. The carrier concentrations determined here are broadly comparable with those determined by Li *et al.*[68] for $Cu_{1-y}Fe_{1+y}S_2$ at similar Cu : Fe ratios. However, the latter reports a much wider range of Cu : Fe ratios obtained by Cu/Fe substitution than those resulting from the formation of microprecipitates. While the carrier concentration reported by Li *et al.*[68] varies monotonically with the nominal value of y, the variation with the analytically determined Cu : Fe ratio is less systematic. At much lower Cu : Fe ratios ($\lesssim 0.90$) the charge-carrier concentration reaches values which are an order of magnitude higher than the maximum value determined here. The carrier mobility has a weaker correlation with the Cu : Fe ratio. This is likely to be due to a combination of the change in the Cu : Fe ratio and the nanometre length scale of the $[Cu,Fe,Cr]_3S_4$ precipitates, which may be responsible for scattering electrons with comparable mean-free paths,[69] thereby

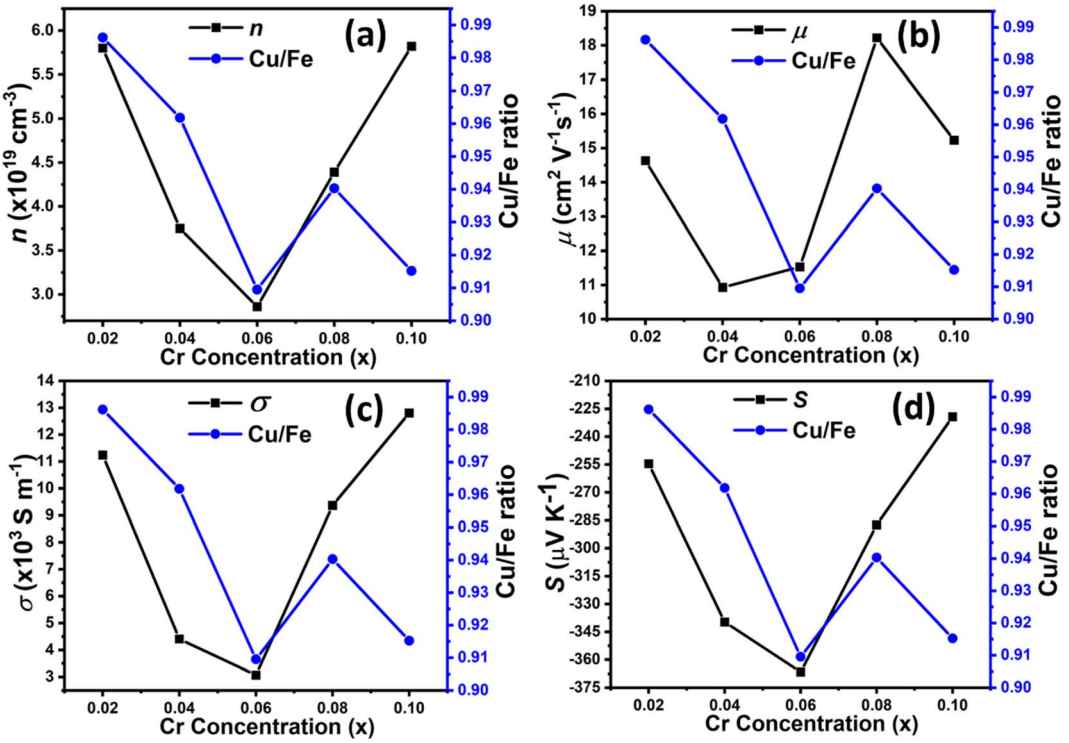

Fig. 6 The relationship (at 323 K) between (a) carrier concentration (n), (b) carrier mobility (μ), (c) electrical conductivity ($\sigma = 1/\rho$), (d) Seebeck coefficient (S) and the Cu : Fe ratio of the main $CuFeS_2$ phase in samples of nominal composition $Cu_{1-x}Cr_xFeS_2$, presented as a function of the nominal chromium content (x).

affecting the carrier mobility, and hence resulting in the trends in Hall mobilities presented in Fig. 5. The $[Cu,Fe,Cr]_3S_4$ thiospinels are semiconductors, although the magnitude of the resistivity and Seebeck coefficient are highly composition dependent.[54,55] The former spans two orders of magnitude and the latter shows a change from n- to p-type behaviour. Since the thiospinel microprecipitates are present at a level of <5 vol%, we believe they have limited impact on the electrical transport properties of the bulk materials, beyond the impact on mobility noted above.

Fig. 7 shows the electrical properties of $Cu_{1-x}Cr_xFeS_2$ ($0 \leq x \leq 0.1$) as a function of temperature. All the Cr-containing samples show a decrease in the electrical resistivity (ρ) compared to that of $CuFeS_2$. In addition, the temperature dependence of the electrical resistivity of $Cu_{1-x}Cr_xFeS_2$ ($0.02 \leq x \leq 0.1$) shows a marked change, with $\rho(T)$ becoming flatter compared to the parent $CuFeS_2$. Similar behaviour has been observed previously in substituted chalcopyrites.[29,30] The lowest electrical resistivity exhibited by compositions with $x = 0.02$, 0.08 and 0.1 is reduced by more than 70% from that of $CuFeS_2$. Whilst the resistivity for compositions with $x = 0.04$ and 0.06 is higher, which appears to be associated with both lower carrier concentration and mobility, it remains below that of the parent phase. The Seebeck coefficient (S) shows a similar behaviour as S is reduced from that of $CuFeS_2$ in all the Cr-containing materials. However, the reduction in the magnitude of the Seebeck coefficients in the Cr-containing materials is less marked than the reductions in the electrical resistivity, particularly for the compositions with $x = 0.02$ and 0.08. Consequently, the power factor (PF) exhibited by the Cr-containing materials is significantly higher than that of the pristine $CuFeS_2$. The highest PF = 0.77 mW m^{-1} K^{-2} at 673 K is exhibited by the composition with $x = 0.08$. It can be seen from Fig. 6 that the electrical transport properties show a strong correlation with the Cu : Fe ratio, and therefore, the formation of the spinel precipitates. The behaviour of the composition with $x = 0.1$, is slightly anomalous, which may be the result of complex compositional variations in the main and spinel secondary phases.

Fig. 8 presents the thermal conductivity of $Cu_{1-x}Cr_xFeS_2$ ($0 \leq x \leq 0.1$). The total thermal conductivity (κ) is dominated by the lattice contribution (κ_L) at all compositions. This is relatively high for the pristine $CuFeS_2$ phase (*ca.* 6.7 W m^{-1} K^{-1} at 323 K), as reflected in the high average sound velocity of 3264 m s^{-1} (Table 1), facilitated by the strong covalent bonding within the diamond-like structure of the chalcopyrite. On chromium incorporation, there is a marked reduction of *ca.* 40% in the lattice thermal conductivity for materials with compositions $x =$ 0.02, 0.08 and 0.1. This is also reflected in the average (v_{avg}), mean (v_m), longitudinal (v_l) and transverse (v_t) sound velocities whose dependence on compositions correlates closely with that of the lattice thermal conductivity, as seen in Table 1. Although Li *et al.*[17] have achieved a slightly lower thermal conductivity (κ = 1.83 W m^{-1} K^{-1} at 300 K) in the sulfur-deficient phase $CuFeS_{1.75}$, it has been pointed out by Lefèvre and co-workers[28] that this level of sulfur deficiency corresponds to compositions

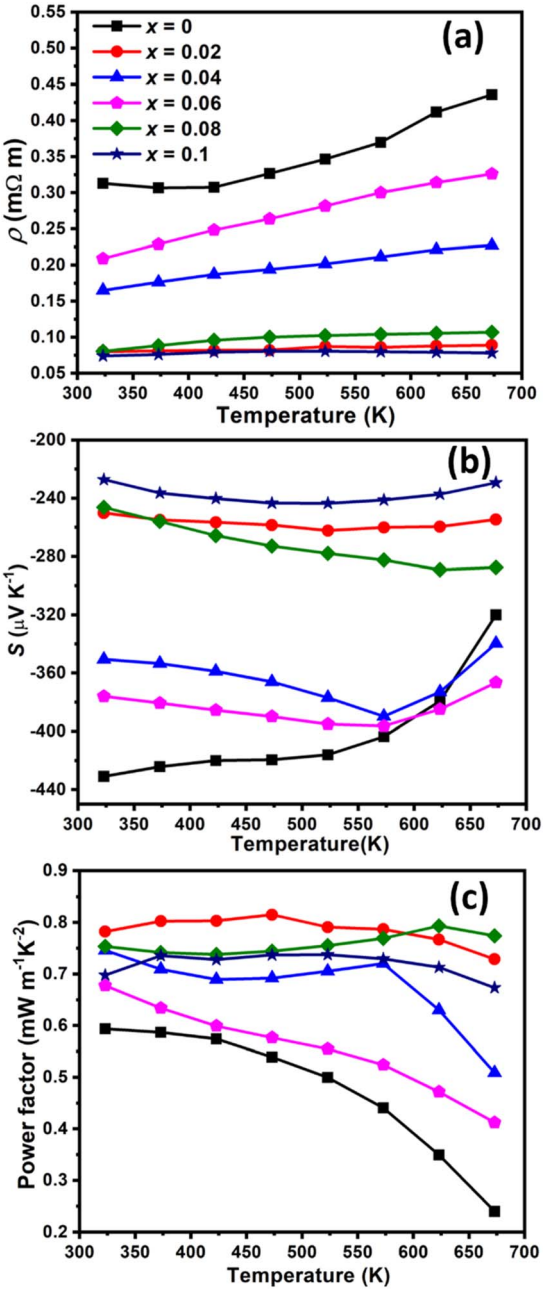

Fig. 7 Temperature dependent (a) electrical resistivity (ρ), (b) Seebeck coefficient (S) and (c) power factor of $Cu_{1-x}Cr_xFeS_2$ ($0 \leq x \leq 0.1$) samples. Uncertainties in electrical resistivity, and Seebeck coefficient are estimated to be *ca.* 5%.

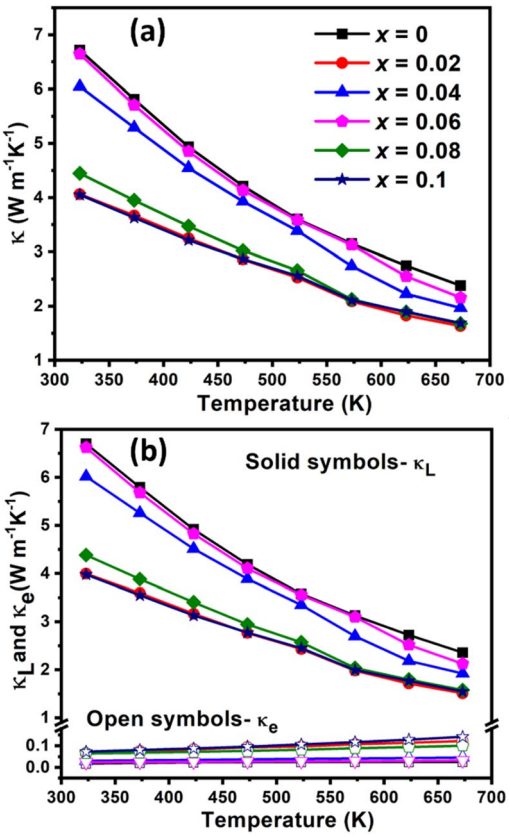

Fig. 8 Temperature dependent (a) total thermal conductivity (κ); (b) lattice (κ_L) and electronic (κ_e) thermal conductivities of $Cu_{1-x}Cr_xFeS_2$ ($0 \leq x \leq 0.1$) samples. Uncertainties in the measured thermal conductivity values are estimated to be *ca.* 10%.

where alternative structure types are stabilized. In particular, the composition $CuFeS_{1.75}$ is consistent with the formation of cubic talnakhite, which exhibits a low thermal conductivity. The thermal and electrical transport properties presented by Li *et al.*[17] are in close agreement with those in recent reports of talnakhite.[70,71]

The elastic moduli and Debye temperature, derived from the sound velocity (calculation details in ESI†) decrease with chromium addition, which can be observed at even the lowest level of chromium incorporation (2 at%). The Young's (E) and shear moduli (G) of the pristine $CuFeS_2$ ($x = 0$) decrease on the introduction of chromium; that for the composition, $x = 0.08$, being *ca.* 30% lower than for the pristine phase. This indicates considerable lattice softening, which may partly contribute to the reduction of the lattice thermal conductivity. It has been shown previously in chalcopyrite-type phases that the mean-free-path of the heat-carrying acoustic phonons lies in the range 50 to 500 nm.[29,36] The SEM and HRTEM images (Fig. 3 and 4) show that the $[Cu, Fe, Cr]_3S_4$ spinel precipitates have a wide range of length scales ranging between 300 nm and 20 μm. Moreover, the HRTEM images also reveal dislocations with length scales in the range 2–50 nm, similar to those previously observed in substituted chalcopyrites.[29,30] A combination of the spinel precipitates and dislocations, therefore, results in the scattering of a wide range of heat-carrying acoustic phonons, leading to a reduced lattice thermal conductivity.

The maximum thermoelectric figure-of-merit of the $Cu_{1-x}Cr_xFeS_2$ ($0 \leq x \leq 0.1$) materials (Fig. 9) increases from $zT = 0.08$ for the parent phase ($x = 0$) to $zT = 0.31$ for the composition with $x = 0.08$ at 673 K. This represents a more than a three-fold increase and is comparable to some of the best figures of merit reported in chalcopyrites.[23,24,26,28,29,72] This improvement in performance is due to a combination of increases in the power factor arising from changes in charge-carrier concentration,

Table 1 Lattice thermal conductivity (κ_L), the average (v_{avg}), mean (v_m), longitudinal (v_l) and transverse (v_t) sound velocities; Young's (E) and shear (G) moduli; Debye temperature (θ_D) of $Cu_{1-x}Cr_xFeS_2$ ($x = 0$, 0.02, 0.06 and 0.08) samples

Sample	κ_L at 323 K (W m^{-1} K^{-1})	v_{avg} (m s^{-1})	v_m (m s^{-1})	v_l (m s^{-1})	v_t (m s^{-1})	E (GPa)	G (GPa)	θ_D (K)
$x = 0$	6.7	3264	2831	4720	2536	69.9	26.9	319
$x = 0.02$	4	2934	2579	4170	2316	56.4	22.1	291
$x = 0.06$	6.6	2983	2575	4342	2304	56.9	21.8	291
$x = 0.08$	4.4	2645	2367	3671	2133	46.8	18.8	267

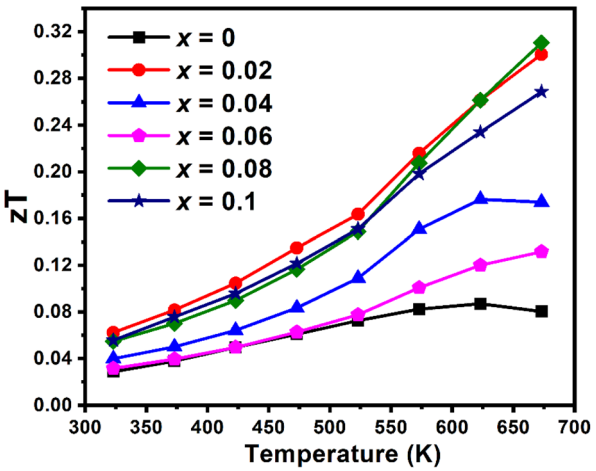

Fig. 9 Thermoelectric figure-of-merit as a function of temperature of $Cu_{1-x}Cr_xFeS_2$ ($0 \leq x \leq 0.1$) samples. Estimated uncertainties in the figures-of-merit (zT) are *ca.* 15%.

induced by variations in the Cu : Fe ratio, and reductions in thermal conductivity due to the formation of precipitates and dislocations spanning a wide range of length scales. The change in the Cu : Fe ratio of the majority chalcopyrite phase correlates with the amount of chromium present in the secondary spinel-type phase and is inversely proportional to the copper content of the spinel phase (Table S3 and Fig. S4†). The trends in electrical- and thermal-transport properties are, therefore, determined indirectly by Cr-induced composite formation and are not a direct result of modification of the electronic structure of the chalcopyrite phase due to substitution of chromium for copper in $CuFeS_2$.

Conclusions

A detailed investigation of $Cu_{1-x}Cr_xFeS_2$ using a combination of advanced analytical techniques (PXRD, XANES, SEM and TEM) has established that chromium addition leads to the formation of a composite in preference to substitution. This consists of precipitates of a Cr-rich, $[Cu, Fe, Cr]_3S_4$ spinel-type phase within a chalcopyrite matrix. The formation of a Cr-rich precipitate, which also contains copper and iron, induces changes to the Cu : Fe ratio of the $CuFeS_2$ chalcopyrite phase. This effects reduction of a fraction of Fe^{3+} cations to Fe^{2+}, altering the carrier concentration of the majority phase and hence, modifying the electrical-transport properties and increasing the power factor. The spinel-type precipitates occur with a wide range of length scales and together with dislocations, promote scattering of heat-carrying phonons over a correspondingly wide range of the phonon spectra and mean free paths (50 to 500 nm), resulting in a significant reduction in lattice thermal conductivity. This leads to a maximum thermoelectric figure-of-merit $zT = 0.31$ at 673 K ($x = 0.08$) that is higher than that of the majority of substituted chalcopyrites, including those containing transition-metal substituents. The present work suggests that the formation within a chalcopyrite matrix, of micro-precipitates involving elements from the parent phase, may offer a means of simultaneously tuning the carrier concentration through modification of the Cu : Fe ratio while increasing phonon scattering by the precipitates. The fact that this may be achieved by standard high-temperature synthesis, without recourse to any special synthesis procedures, such as rapid-cooling/quenching, prolonged thermal treatment or through the intentional addition of a secondary phase/material to form a multi-phasic composite, offers attractions in the development of high-performance thermoelectric materials. However, adjusting the synthesis conditions, including the cooling rate, may offer a means of achieving further enhancements in performance through changes in morphology, dimensions and size distribution of the microprecipitates. Furthermore, double substitution offers opportunities to combine the beneficial impact of microprecipitate formation on thermal conductivity with the capacity to effect changes to electrical-transport properties by varying the charge-carrier concentrations. More detailed studies are required to understand the thermodynamic and kinetic factors that promote precipitation over substitution and in particular, to identify alternative transition-metal cations with limited solubility in chalcopyrite and other complex metal chalcogenides.

Author contributions

The manuscript was written through contributions of all authors. All authors have given approval to the final version of the manuscript.

Conflicts of interest

There are no conflicts to declare.

Acknowledgements

This work was carried out with the support of the UK Engineering and Physical Sciences Research Council, through the

UKRI Global Challenges Research Fund (grant no: EP/T020040/1). The authors acknowledge Diamond Light Source Ltd, UK for beamtime on B18 beamline under proposal no: SP30136. We would also like to thank the Chemical Analysis Facility (CAF) at the University of Reading, Reading, UK.

References

1 R. Freer and A. V. Powell, *J. Mater. Chem. C*, 2020, **8**, 441–463.
2 A. V. Powell, *J. Appl. Phys.*, 2019, **126**, 100901.
3 S. Tippireddy, A. V Powell and T. K. S. Wong, in *Sulfide and Selenide Based Materials for Emerging Applications*, Elsevier, 2022, pp. 329–376.
4 R. Freer, D. Ekren, T. Ghosh, K. Biswas, P. Qiu, S. Wan, L. D. Chen, S. Han, C. Fu, T.-J. Zhu, A. K. M. A. Shawon, A. Zevalkink, K. Imasato, G. J. Snyder, M. Ozen, K. Saglik, U. Aydemir, R. Cardoso-Gil, E. Svanidze, R. Funahashi, A. V. Powell, S. Mukherjee, S. Tippireddy, P. Vaqueiro, F. Gascoin, T. Kyratsi, S. Philipp and T. Mori, *J. Phys.: Energy*, 2022, **4**, 022002.
5 L. Paradis-Fortin, G. Guélou, V. Pavan Kumar, P. Lemoine, C. Prestipino, O. Merdrignac-Conanec, G. R. Durand, S. Cordier, O. I. Lebedev and E. Guilmeau, *J. Alloys Compd.*, 2020, **831**, 154767.
6 K. Suekuni, F. S. Kim, H. Nishiate, M. Ohta, H. I. Tanaka and T. Takabatake, *Appl. Phys. Lett.*, 2014, **105**, 132107.
7 C. Candolfi, G. Guélou, C. Bourgès, A. R. Supka, R. A. R. al Orabi, M. Fornari, B. Malaman, G. le Caër, P. Lemoine, V. Hardy, J.-M. Zanotti, R. Chetty, M. Ohta, K. Suekuni and E. Guilmeau, *Phys. Rev. Mater.*, 2020, **4**, 025404.
8 R. Chetty, Y. Kikuchi, Y. Bouyrie, P. Jood, A. Yamamoto, K. Suekuni and M. Ohta, *J. Mater. Chem. C*, 2019, **7**, 5184–5192.
9 S. O. J. Long, A. V. Powell, P. Vaqueiro and S. Hull, *Chem. Mater.*, 2018, **30**, 456–464.
10 X. Lu, D. T. Morelli, Y. Xia and V. Ozolins, *Chem. Mater.*, 2015, **27**, 408–413.
11 S. Tippireddy, R. Chetty, M. H. Naik, M. Jain, K. Chattopadhyay and R. C. Mallik, *J. Phys. Chem. C*, 2018, **122**, 8735–8749.
12 S. He, Y. Luo, L. Xu, Y. Wang, Z. Han, X. Li and J. Cui, *Inorg. Chem.*, 2021, **60**, 11120–11128.
13 J. Corps, P. Vaqueiro, A. Aziz, R. Grau-Crespo, W. Kockelmann, J. C. Jumas and A. V. Powell, *Chem. Mater.*, 2015, **27**, 3946–3956.
14 B. Ge, J. Hu, Z. Shi, H. Wang, H. Xia and G. Qiao, *Nanoscale*, 2019, **11**, 17340–17349.
15 B. Du, R. Zhang, K. Chen, A. Mahajan and M. J. Reece, *J. Mater. Chem. A*, 2017, **5**, 3249–3259.
16 C. Bourgès, P. Lemoine, O. I. Lebedev, R. Daou, V. Hardy, B. Malaman and E. Guilmeau, *Acta Mater.*, 2015, **97**, 180–190.
17 J. Li, Q. Tan and J. F. Li, *J. Alloys Compd.*, 2013, **551**, 143–149.
18 L. D. Zhao, H. J. Wu, S. Q. Hao, C. I. Wu, X. Y. Zhou, K. Biswas, J. Q. He, T. P. Hogan, C. Uher, C. Wolverton, V. P. Dravid and M. G. Kanatzidis, *Energy Environ. Sci.*, 2013, **6**, 3346–3355.
19 Y. Wu, Z. Chen, P. Nan, F. Xiong, S. Lin, X. Zhang, Y. Chen, L. Chen, B. Ge and Y. Pei, *Joule*, 2019, **3**, 1276–1288.
20 C. Zhang, M. de la Mata, Z. Li, F. J. Belarre, J. Arbiol, K. A. Khor, D. Poletti, B. Zhu, Q. Yan and Q. Xiong, *Nano Energy*, 2016, **30**, 630–638.
21 W. H. Shin, J. W. Roh, B. Ryu, H. J. Chang, H. S. Kim, S. Lee, W. S. Seo and K. Ahn, *ACS Appl. Mater. Interfaces*, 2018, **10**, 3689–3698.
22 C. Chang, M. Wu, D. He, Y. Pei, C. F. Wu, X. Wu, H. Yu, F. Zhu, K. Wang, Y. Chen, L. Huang, J. F. Li, J. He and L. D. Zhao, *Science*, 2018, **360**, 778–783.
23 H. Xie, X. Su, G. Zheng, T. Zhu, K. Yin, Y. Yan, C. Uher, M. G. Kanatzidis and X. Tang, *Adv. Energy Mater.*, 2017, **7**, 1601299.
24 W. D. Carr and D. T. Morelli, *J. Electron. Mater.*, 2016, **45**, 1346–1350.
25 N. Tsujii and T. Mori, *Appl. Phys. Express*, 2013, **6**, 043001.
26 J. Navratil, J. Kašparová, T. Plecháček, L. Beneš, Z. Olmrová-Zmrhalová, V. Kucek and Č. Drašar, *J. Electron. Mater.*, 2019, **48**, 1795–1804.
27 B. Ge, J. Hu, Z. Shi, H. Wang, H. Xia and G. Qiao, *Nanoscale*, 2019, **11**, 17340–17349.
28 R. Lefèvre, D. Berthebaud, M. Y. Mychinko, O. I. Lebedev, T. Mori, F. Gascoin and A. Maignan, *RSC Adv.*, 2016, **6**, 55117–55124.
29 S. Tippireddy, F. Azough, Vikram, F. T. Tompkins, A. Bhui, R. Freer, R. Grau-crespo, K. Biswas, P. Vaqueiro and A. V. Powell, *Chem. Mater.*, 2022, **34**, 5860–5873.
30 S. Tippireddy, F. Azough, Vikram, A. Bhui, P. Chater, D. Kepaptsoglou, Q. Ramasse, R. Freer, R. Grau-Crespo, K. Biswas, P. Vaqueiro and A. V. Powell, *J. Mater. Chem. A*, 2022, **10**, 23874–23885.
31 H. Xie, X. Su, S. Hao, C. Zhang, Z. Zhang, W. Liu, Y. Yan, C. Wolverton, X. Tang and M. G. Kanatzidis, *J. Am. Chem. Soc.*, 2019, **141**, 18900–18909.
32 B. Ge, H. Lee, C. Zhou, W. Lu, J. Hu, J. Yang, S.-P. Cho, G. Qiao, Z. Shi and I. Chung, *Nano Energy*, 2022, **94**, 106941.
33 D. Zhang, B. Zhang, Z. Zhou, K. Peng, H. Wu, H. Wang, G. Wang, G. Han, G. Wang, X. Zhou and X. Lu, *Chem. Mater.*, 2021, **33**, 9795–9802.
34 Z. Liu, W. Zhang, W. Gao and T. Mori, *Energy Environ. Sci.*, 2021, **14**, 3579–3587.
35 T. Ghosh, M. Dutta, D. Sarkar and K. Biswas, *J. Am. Chem. Soc.*, 2022, **144**, 10099–10118.
36 N. Sato, P. S. Gan, N. Tsujii and T. Mori, *Appl. Phys. Express*, 2021, **14**, 087002.
37 J. Androulakis, C. H. Lin, H. J. Kong, C. Uher, C. I. Wu, T. Hogan, B. A. Cook, T. Caillat, K. M. Paraskevopoulos and M. G. Kanatzidis, *J. Am. Chem. Soc.*, 2007, **129**, 9780–9788.
38 Y. Gelbstein, B. Dado, O. Ben-Yehuda, Y. Sadia, Z. Dashevsky and M. P. Dariel, *Chem. Mater.*, 2010, **22**, 1054–1058.
39 G. Rogl, A. Grytsiv, M. Falmbigl, E. Bauer, C. Mangler, C. Rentenberger, M. Zehetbauer and P. Rogl, *Acta Mater.*, 2012, **60**, 4487–4495.
40 J. R. Sootsman, J. He, V. P. Dravid, C. P. Li, C. Uher and M. G. Kanatzidis, *J. Appl. Phys.*, 2009, **105**, 083718.

41 A. Bhardwaj and D. K. Misra, *J. Mater. Chem. A*, 2014, **2**, 20980–20989.
42 Y. Cheng, J. Yang, Q. Jiang, D. He, J. He, Y. Luo, D. Zhang, Z. Zhou, Y. Ren and J. Xin, *J. Mater. Chem. A*, 2017, **5**, 5163–5170.
43 B. A. Cook, M. J. Kramer, J. L. Harringa, M. K. Han, D. Y. Chung and M. G. Kanatzidis, *Adv. Funct. Mater.*, 2009, **19**, 1254–1259.
44 S. N. Girard, J. He, C. Li, S. Moses, G. Wang, C. Uher, V. P. Dravid and M. G. Kanatzidis, *Nano Lett.*, 2010, **10**, 2825–2831.
45 Y. Gelbstein, J. Davidow, S. N. Girard, D. Y. Chung and M. Kanatzidis, *Adv. Energy Mater.*, 2013, **3**, 815–820.
46 J. R. Scotsman, R. J. Pcionek, H. Kong, C. Uher and M. G. Kanatzidis, *Chem. Mater.*, 2006, **18**, 4993–4995.
47 A. Bali, E. Royanian, E. Bauer, P. Rogl and R. C. Mallik, *J. Appl. Phys.*, 2013, **113**, 123707.
48 U. ur Rehman, K. Mahmood, A. Ashfaq, A. Ali, S. Tahir, S. Ikram, A. Rehman, K. ul Sahar, W. Ahmad and N. Amin, *Mater. Chem. Phys.*, 2022, **279**, 125765.
49 S. Verma, M. Singh, D. Ahuja, H. Shimose, S. Nishino, M. Miyata, D. Mott, M. Koyano and S. Maenosono, *Jpn. J. Appl. Phys.*, 2014, **53**, 120301.
50 L. Vaure, Y. Liu, D. Cadavid, F. Agnese, D. Aldakov, S. Pouget, A. Cabot, P. Reiss and P. Chenevier, *ChemNanoMat*, 2018, **4**, 982–991.
51 P. Baláž, E. Dutková, P. Levinský, N. Daneu, L. Kubíčková, K. Knížek, M. Baláž, J. Navrátil, J. Kašparová, V. Ksenofontov, A. Möller and J. Hejtmánek, *Mater. Lett.*, 2020, **275**, 128107.
52 P. Baláž, E. Dutková, M. Baláž, R. Džunda, J. Navrátil, K. Knížek, P. Levinský and J. Hejtmánek, *ChemistryOpen*, 2021, **10**, 806–814.
53 E. Agostinelli, D. Fiorani, G. Mattogno and M. Noguess, *J. Phys. Chem. Solids*, 1989, **50**, 269–272.
54 E. M. Zub and S. V. Sukhvalo, *Solid State Commun.*, 1987, **64**, 989–992.
55 E. M. Zub, E. V. Kuchis and S. V. Sukhvalo, *Phys. Status Solidi A*, 1984, **82**, 569.
56 A. V. Powell and S. Oestreich, *J. Mater. Chem. A*, 1996, **6**, 807–813.
57 A. V. Powell, D. C. Colgan and C. Ritter, *J. Solid State Chem.*, 1997, **134**, 110–119.
58 H. Groß, D. Groeneveld, M. Poschmann, U. Schürmann, J. D. König, W. Bensch, J. Wöllenstein and L. Kienle, *Adv. Eng. Mater.*, 2023, **25**, 2201505.
59 E. V. Korotaev, M. M. Syrokvashin, I. Y. Filatova and V. V. Zvereva, *Vacuum*, 2020, **179**, 109390.
60 J. Rodríguez-Carvajal, in *Abstracts of the Satellite Meeting on Powder Diffraction of the XV Congress of the IUCr*, Toulouse, France, 1990, p. 127.
61 A. J. Dent, G. Cibin, S. Ramos, S. A. Parry, D. Gianolio, A. D. Smith, S. M. Scott, L. Varandas, S. Patel, M. R. Pearson, L. Hudson, N. A. Krumpa, A. S. Marsch and P. E. Robbins, *J. Phys.: Conf. Ser.*, 2013, **430**, 012023.
62 B. Ravel and M. Newville, *J. Synchrotron Radiat.*, 2005, **12**, 537–541.
63 H. Xie, X. Su, S. Hao, C. Zhang, Z. Zhang, W. Liu, Y. Yan, C. Wolverton, X. Tang and M. G. Kanatzidis, *J. Am. Chem. Soc.*, 2019, **141**, 18900–18909.
64 I. Nakai, Y. Sugitani, K. Nagashima and Y. Niwa, *J. Inorg. Nucl. Chem.*, 1978, **40**, 789–791.
65 A. Ghahremaninezhad, D. G. Dixon and E. Asselin, *Electrochim. Acta*, 2013, **87**, 97–112.
66 S. Gorsse, P. Bellanger, Y. Brechet, E. Sellier, A. Umarji, U. Ail and R. Decourt, *Acta Mater.*, 2011, **59**, 7425–7437.
67 T. Ikeda, L. A. Collins, V. A. Ravi, F. S. Gascoin, S. M. Haile and G. J. Snyder, *Chem. Mater.*, 2007, **19**, 763–767.
68 Y. Li, T. Zhang, Y. Qin, T. Day, G. J. Snyder, X. Shi and L. Chen, *J. Appl. Phys.*, 2014, **116**, 203705.
69 J. Park, Y. Xia and V. Ozoliņš, *J. Appl. Phys.*, 2019, **125**, 125102.
70 H. Xie, X. Su, X. Zhang, S. Hao, T. P. Bailey, C. C. Stoumpos, A. P. Douvalis, X. Hu, C. Wolverton, V. P. Dravid, C. Uher, X. Tang and M. G. Kanatzidis, *J. Am. Chem. Soc.*, 2019, **141**, 10905–10914.
71 S. Mukherjee, A. V. Powell, D. J. Voneshen and P. Vaqueiro, *J. Solid State Chem.*, 2022, **314**, 123425.
72 H. Xie, X. Su, G. Zheng, Y. Yan, W. Liu, H. Tang, M. G. Kanatzidis, C. Uher and X. Tang, *J. Phys. Chem. C*, 2016, **120**, 27895–27902.

